Reversible superdense ordering of lithium between two graphene sheets

Kühne, M.; Börrnert, F.; Fecher, S.; Ghorbani-Asl, M.; Biskupek, J.; Samuelis, D.; Krasheninnikov, A. V.; Kaiser, U.; Smet, J. H.;

Reversible superdense ordering of lithium between two graphene sheets

Matthias Kühne[1]*, Felix Börrnert[2]*, Sven Fecher[1], Mahdi Ghorbani-Asl[3], Johannes Biskupek[2], Dominik Samuelis[1]†, Arkady V. Krasheninnikov[3,4,5], Ute Kaiser[2] & Jurgen H. Smet[1]

[1] *Max Planck Institute for Solid State Research, 70569 Stuttgart, Germany.*

[2] *Materialwissenschaftliche Elektronenmikroskopie, Universität Ulm, 89081 Ulm, Germany.*

[3] *Institute of Ion Beam Physics and Materials Research, Helmholtz-Zentrum Dresden-Rossendorf, 01328 Dresden, Germany.*

[4] *Department of Applied Physics, Aalto University, 00076 Aalto, Finland.*

[5] *National University of Science and Technology MISiS, 119049 Moscow, Russia.*

† *Present address: Heraeus Battery Technology, 63450 Hanau, Germany.*

* *These authors contributed equally to this work.*

Many carbon allotropes can act as host materials for reversible lithium uptake,[1,2] laying the grounds for existing and future electrochemical energy storage. Insights into exactly how lithium is arranged within those are, however, challenging to obtain *in operando*. Using *in situ* transmission electron microscopy (TEM)[3-5] to probe light elements (especially Li) [6,7] is severely hampered by their low scattering cross section for impinging electrons and their susceptibility to knock-on damage[8]. Here, we study the reversible Li intercalation of bilayer graphene by *in situ* spherical and chromatic aberration-corrected low-voltage TEM[9], supported by electron energy loss spectroscopy (EELS) and density functional theory (DFT) calculations. Upon their remote insertion from an electrochemical gate, we observe Li atoms to assume multi-layered close-packed order between the two carbon

23 **sheets. The associated Li storage capacity by far exceeds the one of LiC_6—the densest**

24 **configuration known under normal conditions for bulk graphitic carbon[10]. Our findings**

25 **thus point to the possible existence of distinct storage arrangements of ions in 2D layered**

26 **materials as compared to their bulk parent compounds.**

27 Figure 1a shows a schematic of our devices, all of which are supported by Si_3N_4-covered Si

28 substrates. The Si_3N_4 forms a 40×40 μm^2 membrane at the centre of the Si-chip. The bilayer

29 graphene flake is exfoliated from natural graphite and etched into a Hall bar shape. One end of

30 the flake is connected to a counter electrode *via* a Li-ion conducting solid polymer electrolyte.

31 This setup allows for the controlled electrochemical reduction/oxidation of bilayer graphene

32 according to[1]

$$x\text{Li}^+ + x\text{e}^- + \text{C}_n \rightleftharpoons \text{Li}_x\text{C}_n. \tag{1}$$
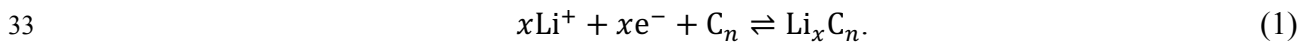
34 Similar to Refs. [11, 12], we trigger lithiation (delithiation) by applying a positive voltage $U_G =$

35 5 V ($U_G = 0$ V) to the counter electrode with respect to bilayer graphene. A grounded current

36 lead to the latter serves as a source/sink for electrons required to facilitate the reversible

37 intercalation of Li-ions at the electrolyte-covered end of bilayer graphene. Intercalated Li

38 exhibits rapid lateral diffusion that tends to establish and maintain an even distribution of Li

39 throughout the bilayer.[13] Hence, one may study its ordering in a region well separated from the

40 electrolyte by *in situ* TEM (Figs. 1a–b), thereby also preventing exposure of the electrolyte to

41 the electron beam. In the region probed by TEM, bilayer graphene is suspended over a hole in

42 the Si_3N_4 membrane. Metallic contacts to the bilayer allow monitoring its resistivity $\rho_{xx} =$

43 U_{xx}/I in the electrolyte-uncovered region (Fig. 1a). During subsequent lithiation/delithiation

44 cycles, we typically observe reversible changes in ρ_{xx} (Fig. 1c). These relate to changes in the

45 local Li concentration *via* finite electronic charge transfer.[12,13] The drop in ρ_{xx} during lithiation

46 reflects an increase in electron density, characteristic for ambipolar diffusion of electron-ion

47   pairs into the probed area.[13] During delithiation, Li-ions and electrons leave the bilayer, thereby

48   restoring its initial resistivity value. The exact time evolution of ρ_{xx} depends on the kinetics of

49   several (uncontrolled) processes, related to e.g. ionic transport within the electrolyte and across

50   the solid electrolyte interphase. Yet, Fig. 1c is a qualitative characteristic of reversible Li

51   intercalation in bilayer graphene.[13] In the following, we present *in situ* TEM data obtained in the

52   *SALVE* (Sub-Ångström Low-Voltage Electron microscopy) microscope[9]. We work at an

53   electron acceleration voltage of 80 kV, just below the threshold for knock-on damage of C atoms

54   in graphene.[14] Despite these conditions, the instrument still delivers sub-Ångström resolution in

55   the images. Further details can be found in Methods (also Extended Data Figs. 1–2).

56

57   Figure 2a shows a TEM image of pristine bilayer graphene. The inset depicts its Fourier

58   transform (FT) and confirms the known value of the in-plane lattice constant a_C = 2.46 Å. The

59   image marks the beginning of a series acquired during lithiation of a bilayer graphene device

60   (Figs. 2a–c and Supplementary Video 1), but it is representative of the sample state prior to

61   application of the bias voltage $\boldsymbol{U_G = 5\,V}$. In Fig. 2b, acquired after 170 s, a second crystal lattice

62   has appeared in the lower half of the probed area. White dashed lines demarcate its boundary on

63   the left and right of the image. The image in Fig. 2c is recorded at t = 288 s. The additional

64   crystal structure now extends throughout almost the whole field of view. Fig. 2d is the Fourier

65   transform of Fig. 2b. Compared with the Fourier transform of pristine bilayer graphene (inset to

66   Fig. 2a), we identify three sets of additional signals, highlighted in red, green, and blue. These

67   attest to hexagonal crystalline order (as for graphene), but with an in-plane lattice constant of

68   3.1 Å. In Fig. 2e, their spatial distribution is mapped. This allows discerning three grains none

69   of which are aligned to the encapsulating graphene lattice. In Fig. 2f the same Fourier transform

70   is shown but with a von Hann filter applied to minimize the streaks. The highlighted signals

71   stem from both bilayer graphene (cyan) and the additional crystalline phase (green) as well as

72 Moiré artefacts (magenta) and their origin (bold arrows). Fig. 2g is a Fourier-filtered (Methods

73 and Extended Data Fig. 3) version of panel b, where the graphene lattice, as well as the Moiré

74 effects, have been removed (see panels h and i for a magnification before and after filtering).

75 These images offer a direct view on the encapsulated crystal. The observed contrast in the images

76 also suggests regions of different thickness even within a single grain. This is worked out in

77 detail in Methods and Extended Data Fig. 4.

78

79 To narrow down the chemical composition of the additional crystal structure, EELS data has

80 been acquired on bilayer graphene before and during lithiation (Fig. 2j). Before lithiation, we

81 exclusively observe the C K-edge at 284 eV. During lithiation the Li K-edge at 55 eV on regions

82 characterized by a Fourier transform as in Fig. 2d is additionally detected. Based on the absence

83 of other signals in the explored energy range of 0–800 eV, Si ($L_{2,3}$-edge starting at 99 eV), S

84 ($L_{2,3}$-edge starting at 165 eV), N (K-edge starting at 400 eV), O (K-edge starting at 532 eV and

85 F (K-edge starting at 685 eV) are discarded as significant constituents of the new crystalline

86 phase. Likewise, Ti and Pt (electrode material) can be ruled out based on the observed light

87 atomic contrast in Fig. 2 for the case of Pt and on the absence of the distinct Ti $L_{2,3}$-edge at 456

88 eV in the EELS data. Although it is inherently impossible to exclude H or C, the crystalline

89 phase formed during lithiation likely consists of pure Li. The low onset in energy of the Li K-

90 edge supports this assertion.[15,16] Also, a Li plasmon mode appears near 9 eV[17,18] (Extended Data

91 Fig. 5a). Though the shape of the Li-K edge resembles the one of Li_2O/LiOH,[15,16] stoichiometric

92 Li_2O/LiOH can be disqualified, since we would then expect both a more pronounced O-K edge

93 as well as an imaging contrast comparable in strength to the encapsulating graphene.[19] Good

94 agreement with experiment is attained when calculating the Li-K edge shape of graphene-

95 encapsulated Li multilayers (Methods and Extended Data Fig. 5b). We do not rule out the

96 presence of trace oxygen, also suggested by the occasional observation of a weak shoulder near

97 30 eV (Extended Data Fig. 5a), previously attributed to oxidized lithium.[17,18] Yet, the extracted

98 in-plane lattice constant of 3.1 Å matches close-packed Li.[20] This coincidence is surprising,

99 since normally very low temperatures and/or extreme pressures are required for Li to assume

100 this ordering.[21]

101

102 To test whether indeed the formation of a dense, multi-layered Li crystal in bilayer graphene is

103 conceivable, first-principles calculations were carried out (Methods). The chemical potential of

104 Li atoms in bulk close-packed phases was evaluated. All energies below are given with respect

105 to the hexagonal close-packed (hcp) phase, which had the lowest energy in the calculations.

106 Several layers of Li atoms inside bilayer graphene are considered (Fig. 3 and Extended Data

107 Figs. 6–8). Since the *in situ* TEM studies do not reveal evidence for a change in registry of the

108 graphene sheets (Extended Data Fig. 9), AB stacking is assumed as in the pristine device. Our

109 main conclusions, however, hold irrespective of the stacking order. The relaxation of atomic

110 coordinates of a single layer of Li atoms yields an energetically favoured C_6LiC_6 configuration,

111 with Li arranged in a commensurate $(\sqrt{3}\times\sqrt{3})R30°$ superstructure with a lattice constant of a_{LiC_6}

112 = 4.26 Å (Figs. 3a–b). Except for the graphene registry, this finding is similar to the bulk LiC_6

113 phase[10] and the AA-stacked C_6LiC_6 phase[22]. The situation changes for a larger number of Li

114 layers. Finite clusters and infinite (periodic) hcp structures with different orientation with respect

115 to the graphene lattice were considered (Figs. 3c–f, Extended Data Figs. 7–8). The energies of

116 these systems are very close to that of the C_6LiC_6 configuration (higher by only 0.01–0.05 eV/

117 Li atom). The in-plane lattice constant a_{Li} of the Li hcp bilayer and trilayer (average distances,

118 as the positions of Li atoms are affected by nearby C atoms) is in the range of 3.05–3.15 Å,

119 matching the experimental value of 3.1 Å as well as the identical literature value.[20] These results

120 suggest that the formation of a multilayer close-packed Li phase between graphene sheets is

121 conceivable. Its precise stacking order may however differ from hcp as other configurations are

122 energetically similar (Extended Data Fig. 8d–e). These are hard to distinguish in these TEM

123 experiments, because we may only observe the projection along one crystal direction. Moreover,

124 some bulk diffraction selection rules do not hold in the given case of an atomically thin

125 specimen. TEM image simulations reveal comparable contrast and diffraction patterns for the

126 two extreme cases: cubic close-packed (ccp) and hexagonal close packed (Extended Data Fig.

127 2f–g).

128

129 By analysing the electronic structure and charge distribution, the charge transfer between Li and

130 graphene can be estimated. Fig. 3b,d and f display colour renditions of the charge probability

131 distribution as compared to isolated graphene and Li crystals consisting of a single, double or

132 triple layer. As can be seen from Fig. 3f in the triple layer case, charge transfer is significant

133 only for the outer Li layers directly neighbouring a graphene sheet. Inner Li layers retain their

134 metallic character as electronic charge is distributed between the Li^+ lattice sites. Extended Data

135 Fig. 8c depicts the average charge transfer per Li atom, which drops as the close-packed Li phase

136 gets thicker. Renormalizing by the number of atoms in the outermost Li layers only, we find a

137 constant charge transfer of approximately 0.33 e^-/outer Li atom, irrespective of how many

138 (metallic) Li layers (with nearly zero charge transfer) are packed in between. This is consistent

139 with the observation that the resistivity ρ_{xx} measured during lithiation tends to saturate rather

140 than to decrease progressively as more Li enters bilayer graphene (Fig. 1c). Note that although

141 for C_6LiC_6 (Figs. 3a–b) a higher value of 0.85 e^-/Li atom for the charge transfer applies resulting

142 in an estimated density of transferred electrons of $2.7 \cdot 10^{14}$ cm^{-2} per graphene sheet, the much

143 denser arrangement of Li atoms in the close-packed structure yields a higher electron density

144 per graphene sheet of $4 \cdot 10^{14}$ cm^{-2} despite the smaller charge transfer value.

145

146   During lithiation, the close-packed Li phase grows laterally between the graphene sheets (Fig.

147   4a and Supplementary Video 1). In Fig. 4a, The graphene signals have been Fourier filtered in

148   order to reveal the Li crystal structure. Three grains of varying in-plane orientation have been

149   coloured for the sake of illustration. While the grain boundary between the central grain (green)

150   and the lower right grain (blue) is rather sharp and stable, the one with the left grain (red) appears

151   more fuzzy and mobile as their orientation nearly matches. Regions of different thickness can

152   be identified even within a single grain (Extended Data Fig. 4). The specimen is too thin to

153   reliably extract its exact thickness t from EELS (we typically obtain $t/\lambda < 0.1$, where λ is the

154   inelastic mean free path of our 80 keV electrons). One may nonetheless determine relative

155   variations (see Methods). When imaging an extremely thin slab of weakly scattering elements

156   in a microscope with sufficient resolving power, the imaging contrast does increase with

157   increasing specimen thickness. This is quantified in the Extended Data Figs. 4e–f, revealing that

158   thinner parts of the close-packed Li phase tend to be located closer to its perimeter. At the leading

159   edge, single atoms can be identified (Methods, Extended Data Fig. 1). From the image time

160   series, a lateral growth rate of the order of 1 Å/s can be extracted. During delithiation the close-

161   packed Li phase disassembles and gradually disappears (Fig. 4b). Eventually, the pure bilayer

162   graphene lattice remains behind. The degree of reversibility of this process is limited by the

163   number of defects in the graphene lattice and their irreversible formation during prolonged

164   imaging (electron irradiation). Given the combined slow image acquisition (on the order of 1 s)

165   and low sensitivity to light atoms, Li diffusing at speed in less ordered configuration remains

166   concealed to the TEM observer. Such processes are nonetheless present in parallel with the close

167   packing as well as beyond the boundaries of this phase and are likely responsible for the initial

168   abrupt change in resistivity ρ_{xx} during lithiation (Fig. 1c).

169

170　We note that the observed crystalline phase of Li proves stable between intact graphene planes

171　only. With the incident electron energy exceeding the threshold for displacement damage of Li

172　(~20 keV), conditions are such that Li readily "boils" under the electron beam[16,18]. The close-

173　packed phase is volatile when imaged near bilayer edges or in the presence of a high density of

174　defects in the graphene lattice. Constituents may escape from between graphene sheets *via* such

175　edges or defects upon electron-beam induced melting of the crystalline phase. Likewise, we find

176　material having escaped from within and agglomerated on the outer bilayer surfaces near such

177　defects to quickly evaporate under electron beam irradiation. The protective encapsulation by

178　two impermeable atomic sheets may thus be regarded a prerequisite to safe probing by TEM of

179　the crystal formation therein, akin to the situation in graphene liquid cells[23].

180

181　Close-packing of Li intercalated between graphene sheets, as demonstrated here, results in a

182　structure with Li-content in great excess of LiC_6. Although enhanced Li storage has been

183　proposed to occur on the outside of graphene planes[24,25] previously, suggested atomistic

184　configurations were contradictory among the different works and could neither be addressed nor

185　verified by microscopic means. The same holds for the scarce reports claiming the formation of

186　nanocrystallites of close-packed Li during the lithiation of different carbon allotropes.[26,27] At

187　elevated temperatures, a similar configuration of Li, as we report here, may, as a matter of fact,

188　have been left unidentified in bulk graphite.[28] Since the energy cost for close-packing of Li in

189　the van der Waals gap of bilayer graphene as compared to forming C_6LiC_6 is very similar (Fig.

190　3), close-packing may be the answer of the system for having to accommodate a larger amount

191　of Li supplied within a short time. The activation energy for Li diffusion in bilayer graphene has

192　been calculated (Methods). It points toward facile diffusion of Li between graphene sheets, even

193　in the presence of a close-packed Li phase. Even though, a bilayer can be regarded as the

194　fundamental unit of bulk graphite, it may still feature considerably distinct properties and in

195 particular its layers may spread more easily to accommodate for dense intercalate ordering. It

196 should also be noted that Li-graphite intercalation compounds only occupy a small region in the

197 C-Li binary alloy phase diagram.[29] In the miscibility gap beyond LiC_6, alternative configurations

198 may be available for storing larger amounts of lithium in layered carbons.[30]

199

200 1. Winter, M. & Besenhard, J. O. Lithiated carbons. In *Handbook of Battery Materials* Edn.

201   2 (Daniel, C. & Besenhard, J. O., eds.) 433–478 (Wiley-VCH, Weinheim, Germany,

202   2011).

203 2. Kaskhedikar, N. A. & Maier, J. Lithium storage in carbon nanostructures. *Adv. Mater.* **21**,

204   2664–2680 (2009).

205 3. Zheng, H., Meng, Y. S. & Zhu, Y. Frontiers of in situ electron microscopy. *MRS Bull.* **40**,

206   12–18 (2015).

207 4. Qian, D., Ma, C., More, K. L., Meng, Y. S. & Chi, M. Advanced analytical electron

208   microscopy for lithium-ion batteries. *NPG Asia Mater.* **7**, e193 (2015).

209 5. Liu, X. H. *et al*. In situ TEM experiments of electrochemical lithiation and delithiation of

210   individual nanostructures. *Adv. Energy Mater.* **2**, 722–741 (2012).

211 6. Shao-Horn, Y., Croguennec, L., Delmas, C., Nelson, E. C. & O'Keefe, M. A. Atomic

212   resolution of lithium ions in $LiCoO_2$. *Nat. Mater.* **2**, 464–467 (2003).

213 7. Oshima, Y. & Murakami, Y. (eds.) *Microscopy 66, Number 1, Special Issue: Challenges*

214   *for Lithium Detection* (Oxford University Press Tokyo, Japan, 2017).

215 8. Reimer, L. & Kohl, H. *Transmission Electron Microscopy* (Springer Series in Optical

216   Sciences, Springer, New York, 2008).

217 9. Linck, M. *et al.* Chromatic aberration correction for atomic resolution TEM imaging from

218   20 to 80 kV. *Phys. Rev. Lett.* **117**, 076101 (2016).

219 10. Enoki, T., Suzuki, M. & Endo, M. *Graphite intercalation compounds and applications*

220   (Oxford University Press, New York, 2003).

221 11. Yu, Y. *et al.* Gate-tunable phase transitions in thin flakes of 1T-TaS$_2$. *Nat. Nanotech.* **10**,

222   270–276 (2015).

223 12. Bediako, D. K. *et al.* Heterointerface effects in the electrointercalation of van der Waals

224   heterostructures. *Nature* **558**, 425–429 (2018).

225 13. Kühne, M. *et al.* Ultrafast lithium diffusion in bilayer graphene. *Nat. Nanotech.* **12**, 895–

226   900 (2017).

227 14. Meyer, J. C. *et al.* Accurate measurement of electron beam induced displacement cross

228   sections for single-layer graphene. *Phys. Rev. Lett.* **108**, 196102 (2012).

229 15. Mauchamp, V., Boucher, F., Ouvrand, G. & Moreau, P. Ab initio simulation of the

230   electron energy-loss near-edge structures at the Li K edge in Li, Li$_2$O, and LiMn$_2$O$_4$. *Phys.*

231   *Rev. B* **74**, 115106 (2006).

232 16. Wang, F. *et al.* Chemical distribution and bonding of lithium in intercalated graphite:

233   Identification with optimized electron energy loss spectroscopy. *ACS Nano* **5**, 1190–1197

234   (2011).

235 17. Liu, D.-R. & Williams, D. B. The electron-energy-loss spectrum of lithium metal. *Phil.*

236   *Mag. B* **53**, L123–L128 (1986).

237 18. Hightower, A., Ahn, C. C., Fultz, B. & Rez, P. Electron energy-loss spectrometry on

238   lithiated graphite. *Appl. Phys. Lett.* **77**, 238–240 (2000).

239   19. Liu, X. H. *et al*. In situ transmission electron microscopy of electrochemical lithiation,

240   delithiation and deformation of individual graphene nanoribbons. *Carbon* **50**, 3836–3844

241   (2012).

242   20. Wyckoff, R. W. G. *Crystal structures Vol. 1* Edn. 2 (John Wiley & Sons, 1963).

243   21. Ackland, G. J. *et al*. Quantum and isotope effects in lithium metal. *Science* **356**, 1254–

244   1259 (2017).

245   22. Sugawara, K., Kanetani, K., Sato, R. & Takahashi, T. Fabrication of Li-intercalated

246   bilayer graphene. *AIP Adv*. **1**, 022103 (2011).

247   23. Yuk, J. M. *et al*. High-resolution EM of colloidal nanocrystal growth using graphene

248   liquid cells. *Science* **336**, 61–64 (2012).

249   24. Sato, K., Noguchi, M., Demachi, A., Oki, N. & Endo M. A mechanism of lithium storage

250   in disordered carbons. *Science* **264**, 556–558 (1994).

251   25. Deschamps, M. & Yazami, R. Great reversible capacity of carbon lithium electrode in

252   solid polymer electrolyte. *J. Power Sources* **68**, 236–238 (1997).

253   26. Wang, Q. *et al*. Investigation of lithium storage in bamboo-like CNTs by HRTEM. *J.*

254   *Electrochem. Soc.* **150**, A1281–A1286 (2003).

255   27. Lee, B.-S. *et al*. Face-centered-cubic lithium crystals formed in mesopores of carbon

256   nanofiber electrodes. *ACS Nano* **7**, 5801–5807 (2013).

257   28. Kambe, N. *et al*. Intercalate ordering in first stage graphite-lithium. *Mater. Sci. Eng.* **40**,

258   1–4 (1979).

259   29. Okamoto, H. C-Li (Carbon-Lithium). In *Binary alloy phase diagrams Vol. 1* Edn. 2

260   (Massalski, T. B., Okamoto, H., Subramanian, P. R. & Kacprzak, L., eds.) 857 (ASM

261   International, 1990).

262   30. Lin, D. *et al*. Layered reduced graphene oxide with nanoscale interlayer gaps as a stable

263   host for lithium metal anodes. *Nat. Nanotech*. **11**, 626–632 (2016).

264

276 **Author Contributions** J. H. S and U. K. composed the project. M. K. and S. F. fabricated the

277 samples and performed the electrochemical measurements. F. B. performed the TEM and EELS

278 experiments. M. G. and A. V. K. did the DFT calculations. J. B. helped with TEM and EELS

279 experiments and did TEM imaging simulations. U. K. supervised the TEM work. D. S.

280 contributed to the electrochemical design of the experiment. M. K. and J. H. S. wrote the

281 manuscript and all authors contributed to it.

282 **Author Information** Reprints and permissions information is available at

283 www.nature.com/reprints. The authors declare no competing financial interests. Readers are

284 welcome to comment on the online version of the paper. Correspondence and requests for

285 materials should be addressed to J. H. S. (j.smet@fkf.mpg.de) or U. K. (ute.kaiser@uni-ulm.de).

286
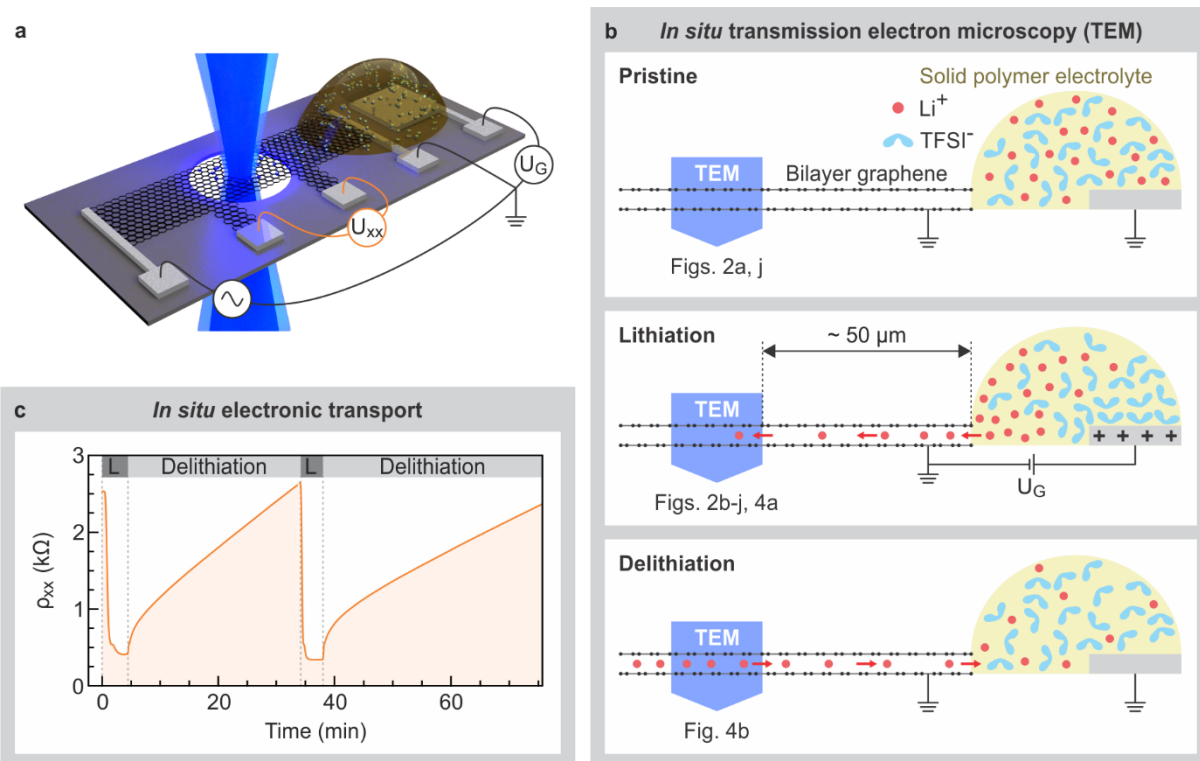
Figure 1 | Device layout and working principle. a, Schematic of the device (not to scale). Bilayer graphene (black) on a substrate (dark grey) is contacted by several metallic electrodes (bright grey). A Li-ion (white spheres) conducting electrolyte (yellow) connects the bilayer with a metallic counter electrode. On the order of 50 µm away from its electrolyte-covered end, bilayer graphene is partially suspended over a hole allowing for transmission electron microscopy (TEM) investigations (electron beam illustrated in blue). **b**, Schematic side view of the pristine device as well as during lithiation and delithiation. Reference to TEM data acquired at the respective state is given. **c**, Bilayer graphene's resistivity ρ_{xx} measured *in situ* during two lithiation (L)/delithiation cycles inside the SALVE microscope with the electron beam blanked. As schematically shown in (**a**), a four point probe configuration serves to reveal reversible changes in the electrolyte-uncovered region of the device.
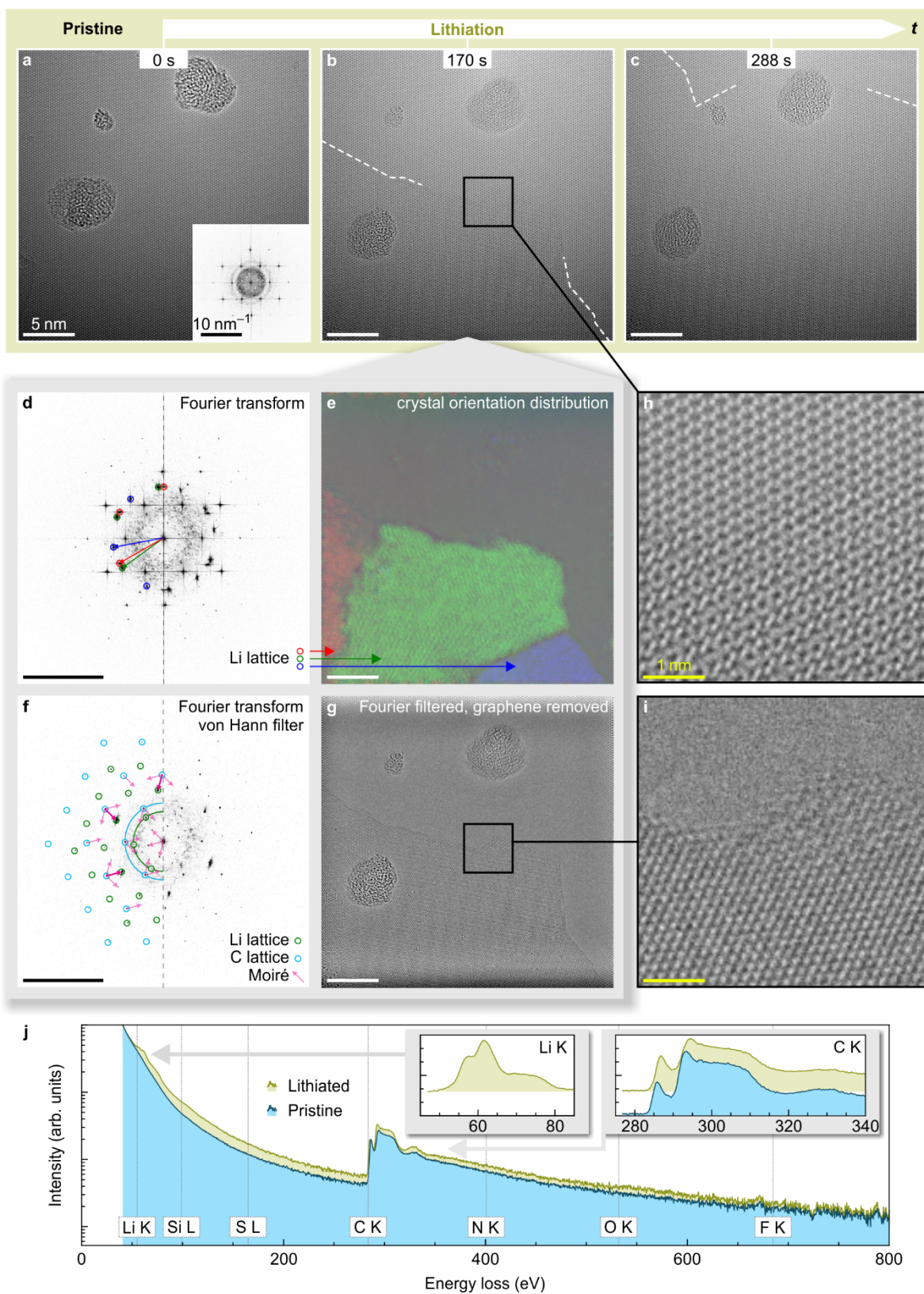
Figure 2 | *In situ* TEM measurements. a–c, TEM images showing the propagating front of a

Li crystal forming inside bilayer graphene during lithiation. The images are acquired on the

same sample area at consecutive times as indicated. Amorphous hydrocarbon adsorbates appear as few nm-large blobs, located above or below the bilayer. The inset in (**a**) is its Fourier transform. **d**, Fourier transform of (**b**). Three sets of spots marked in red, green, and blue are rotated relative to each other as they stem from three different Li crystal grains. The cross-shaped streaks are edge artefacts from the Fourier transform. **e**, Spatial distribution of the Li grains in (**b**) with the colour coding from (**d**). **f**, von Hann-filtered Fourier transform of (**b**). Fourier transforms are point symmetric, therefore, marks on the left side do not mask information. Signals from bilayer graphene (Li) are highlighted in cyan (green); (the origin of) Moiré artefacts are highlighted in (bold) magenta. The anisotropic smearing of the Li signals is due to the sharp propagation front. Signals originating from the grains coloured red and blue in **e** are dampened away by the applied von Hann filter. Half circles represent the fundamental periodicities of 0.213 nm for graphene (cyan) and 0.276 nm for Li (green). **g**, Fourier-filtered version of (**b**) where the graphene lattice, as well as the Moiré effects, are filtered out and only the Li crystal structure is left. The contrast at the edge of the figure is an artefact from the Fourier filter. **h**, **i**, Magnified detail from the demarcated areas in **b** and **g** respectively, showing the Li crystal edge. Scale bars of equal size are coloured identically but labelled only once in (**a**–**g**). **j**, EELS data with logarithmic intensity scale before (blue) and during (yellow) lithiation acquired on an area as in (**a**) and (**c**), respectively. Highlighted are the energies of the relevant major edges. Insets show the near-edge structure of the Li and C K-edges on a linear intensity scale and after individual subtraction of an inverse-power law background. Note that EELS data get noisy at high energies because of the exponential decay of the signal.

322
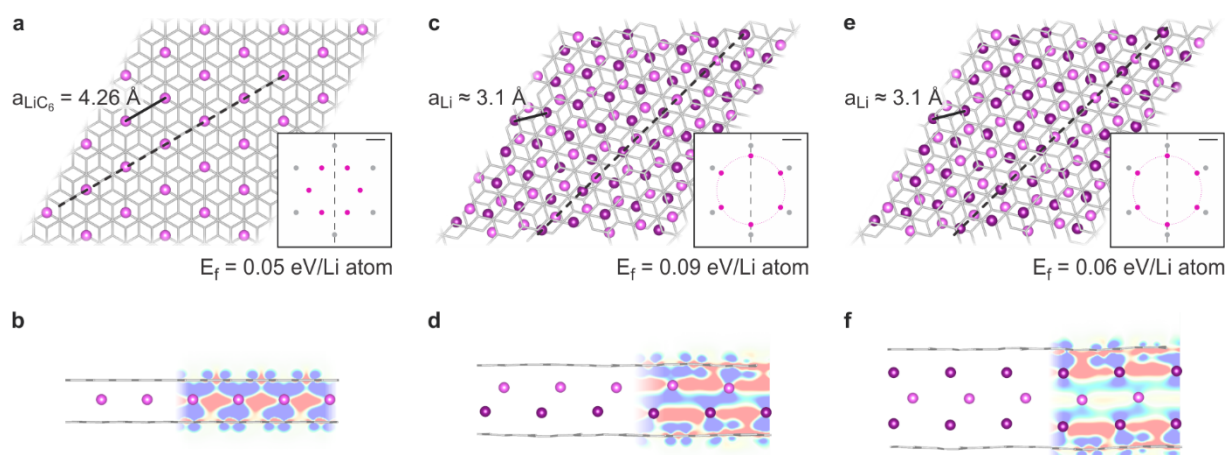
Figure 3 | Atomistic models of Li crystals between AB-stacked graphene sheets obtained from DFT calculations. a, **b**, The 'conventional' C_6LiC_6 configuration with Li arranged in a commensurate $(\sqrt{3}\times\sqrt{3})R30°$ superstructure between graphene sheets. **c**, **d**, Fully optimized bilayer Li crystal. **e**, **f**, Fully optimized trilayer Li crystal (one of two energetically close stacking configurations, compare with Extended Data Fig. 8d). The projection of the latter two structures matches well the experimental observations. (**a**, **c**, **e**) are top views and (**b**, **d**, **f**) are side views along the dashed line given in the respective top view. C atoms and sp^2-bonds are grey, Li atoms are magenta. The insets in (**a**, **c**, **e**) schematically show diffraction patterns associated with the respective structure (scale bar is 2 nm^{-1}), with first order diffraction spots from the Li (C) lattice indicated in magenta (grey). The close-packed Li phase in (**c**, **e**) may assume any relative rotation angle with respect to the bilayer graphene lattice at virtually no additional energy cost (see Extended Data Fig. 7b). A faint magenta circle indicates that the Li diffraction spots may therefore be rotated with respect to those of graphene. E_f is the energy required to take a Li atom from a bulk Li crystal and insert it between graphene sheets in the corresponding configuration. Contour plots in (**b**, **d**, **f**) represent the charge transfer between Li and graphene as compared to the isolated graphene and Li crystals. An increase in the electron density (negative charge) is blue, and a decrease in the electron density (positive charge) is red. Note the smaller average charge transfer to graphene for the multilayer Li crystals.
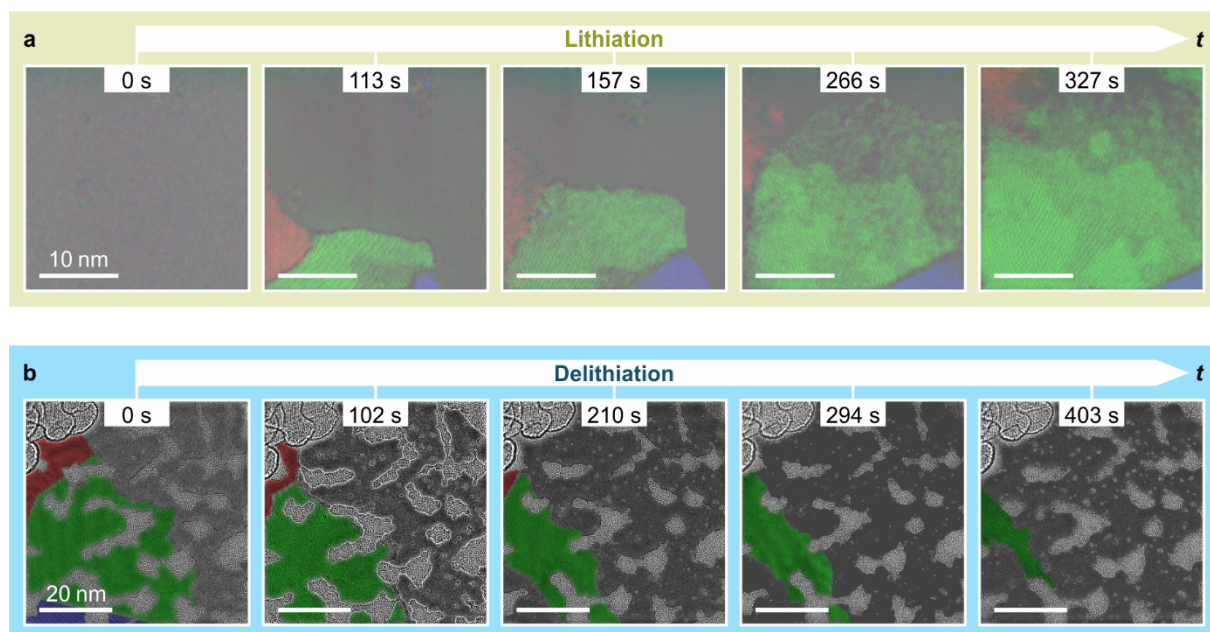
Figure 4 | Li crystal growth between two graphene sheets. a, **b**, Time series of TEM images after Fourier filtering of the bilayer graphene signal acquired during (**a**) lithiation and (**b**) delithiation. Crystal grains of different in-plane orientation are coloured in red, green, and blue. An increased amount of amorphous, immobilized residues (grey areas, essentially composed of carbon) are present within the field of view in (**b**), an unavoidable consequence of extended electron beam illumination. In both (**a**, **b**) the interface with the electrolyte (not contained in the images) is oriented towards the bottom of the page.